Real-space imaging of thermally and photoinduced phase transition in quasi-one-dimensional organic complexes

Keiki Fukumoto [*] and Elizaveta Pyatenko [†]
Institute of Materials Structure Science, High Energy Accelerator Research Organization (KEK), 1-1 Oho, Tsukuba, Ibaraki 305-0801, Japan

Ken Onda and Takanori Tanaka
Department of Chemistry, Kyushu University, 744 Motooka, Nishi-ku, Fukuoka 819-0395, Japan

Koichi Kusakabe
Department of Material Science, Graduate School of Science, University of Hyogo, 3-2-1, Kouto, Kamigori-cho, Ako-gun, Hyogo 678-1297, Japan

Hideki Yamochi
Division of Chemistry, Graduate School of Science, Kyoto University, Sakyo-ku, Kyoto 606-8502, Japan

Shin-ichi Adachi
High Energy Accelerator Research Organization (KEK), 1-1 Oho, Tsukuba, Ibaraki 305-0801, Japan

Shin-ya Koshihara
Department of Chemistry, School of Science, Institute of Science Tokyo, 2-12-1 Ookayama, Meguro-ku, Tokyo 152-8551, Japan

(Received 29 April 2026; accepted 22 July 2026; published 17 September 2026)

Photoinduced phase transition (PIPT) involves substantial changes in both electronic and crystallographic structures caused by electron excitations. Because PIPT is ultrafast and exhibits inhomogeneous behavior, its fundamental processes, in particular, how the ultrafast dynamics of photoexcited electrons trigger lattice deformation and the timescales involved, remain poorly understood. In this study, phase transition and its spatial separation in organic charge-transfer complexes was investigated using photoemission electron microscopy with femtosecond pulsed laser excitation. First, the thermally induced phase transition was confirmed by imaging the morphology change and also by observing the change of spectral shape around the Fermi level. Second, the escape time of photoexcited electrons or the heat generated by the laser pulses is estimated by observing the morphology change depending on the laser repetition rate. Finally, the dynamics of the photoexcited electrons and the subsequent morphology change are directly visualized. The results show that an anisotropic morphology change is initiated following the accumulation of electrons in unoccupied states over approximately a picosecond.

DOI: 10.1103/22k3-7nym

I. INTRODUCTION

In strongly correlated electron-lattice systems exhibiting Mott, Peierls, or charge-ordering transitions, the electronic properties can be changed significantly by external stimuli, leading to phase and/or crystallographic transitions. When such changes are induced by photoabsorption, the phenomenon is known as photoinduced phase transition (PIPT) [1]. PIPT is an attractive phenomena because of its drastic change of materials properties in an ultrafast timescale on the order of femtoseconds to picoseconds, and can be used for future applications such as ultrafast photoswitching devices [2,3], ultrafast memory devices [4], actuators, and sensors [5,6]. Although many studies have been conducted to unravel the mechanism of PIPT, how the photoexcited electrons trigger PIPT remains inadequately understood. This is primarily because photoelectron emission experiments are generally not feasible for insulators (see Fig. S1 of the Supplemental Material [7]). Also, the timescale of these dynamics remains unknown.

To clarify the PIPT phenomenon, ultrafast imaging techniques have been developed and applied to inorganic materials. Using dark-field transmission electron microscopy, Danz *et al.* imaged the structural transitions in a 1T-TaS_2 film [8], and using x-ray free electron lasers, Johnson *et al.* imaged

[*]Contact author: keiki@post.kek.jp
[†]Present address: The Institute for Solid State Physics, The University of Tokyo, 5-1-5 Kashiwanoha, Kashiwa, Chiba 277-8581, Japan.

phase transitions in a VO_2 film via coherent diffraction combined with absorption spectra [9]. Also, the coexistence of the metal and insulator phases in VO_2 on an ultrafast timescale has been captured using time-resolved near-field microscopy, which is sensitive to conducting electrons [10]. On the other hand, there have been no reports of imaging PIPT in organic materials despite their drastic crystallographic change (e.g., Refs. [5,6]), largely because of their low light-absorption damage threshold and inherent softness, which makes them susceptible to fragmentation upon substantial crystallographic changes.

In this study, we performed femtosecond photoemission electron microscopy (fs-PEEM) experiments [11,12] to investigate PIPT in an organic single crystal of $(EDO\text{-}TTF)_2PF_6$, which exhibits strong electron-lattice and electron-electron correlations; in this compound, EDO-TTF (ethylene-dioxytetrathiafulvalene) is the electron donor, while PF_6 is the acceptor. This organic single crystal undergoes first-order metal-to-insulator transition driven by multi-instability that involves mainly charge ordering, accompanied by a significant volume change due to the molecular deformation of EDO-TTF and unit-cell doubling at near room temperature ($T_c \sim 279$ K) [13,14]. Using fs-PEEM, the dynamics of photoexcited electrons and the subsequent PIPT, including spatial phase separation and morphology change, were imaged with temporal and spatial resolutions of 100 fs and 100 nm, respectively. The underlying mechanism was explained by our *ab initio* simulations. After photoabsorption, the photoexcited electrons relax into upper unoccupied states (i.e., the σ antibonding band that shapes the framework of the molecule) within 1.3 ps via electron-phonon thermalization. This accumulation of excited electrons induces an increase in the internal energy, and the C=C bonds that connect the sulfur rings at the middle of the EDO-TTF molecule are stretched. This imbalance of the interatomic forces causes a local structural transformation, such as flattening and translational motion of EDO-TTF and rotation of PF_6, as also observed previously [15]. This results in the band structure turning into the metallic phase and a change in the volume. Subsequently, the system enters a diffusive heating mode, which lasts for longer than 20 ps.

Prior to the time-resolved experiments, the thermally induced phase transition was visualized using PEEM to confirm that the morphology change is a good indicator of the phase transition. Furthermore, we have clarified that the phase transition can also be induced by accumulation of photoexcited electrons by imaging the dependency of the volume change on the laser repetition rate.

II. THERMALLY INDUCED PHASE TRANSITION

Figure 1 shows the phase transition process during cooling of the $(EDO\text{-}TTF)_2PF_6$ single-crystal specimen. The excitation source was a Hg discharge lamp ($h\nu = 4.9$ eV), and the specimen temperature was decreased gradually from 269 to 265 K over 300 s, with the PEEM images stored every 1 s (see Movie S1 in the Supplemental Material [7] for an associated movie). Characterized by volume change or cracking, the structural transition was observed at ca. 267 K, and Figs. 1(a)–1(e) show representative images taken during the transition; the relevant temperatures are shown at the top left of each image. The transition temperature observed in this experiment is lower than that reported in Refs. [13,14]. This may be due to the following reasons. First, the temperature sensor was not directly attached to the specimen, but rather to a metal holder. Specifically, irradiation by a Hg discharge lamp increased the temperature at the specimen surface, which could not be monitored. Additionally, the effect of supercooling should be considered; the lower cooling rate may have caused the phase transition to occur at a lower temperature (see Fig. S2 of the Supplemental Material [7]). At 266.96 K, the specimen started to crack inhomogeneously, and the phase transition was completed within a range of 0.1 K. Figure 1(f) shows the change of photoelectron emission (PE) intensity in the red and green rectangles marked in the PEEM images. The PE intensity decreases when the cracking happens, indicating the switch from the metallic phase to the insulator phase. The sudden jump in PE intensity around 267 K could be due to PE from the edges of the flakes, which is not related to the phase transition.

Conversely, during the heating process, the phase transition occurs at a higher temperature and over a broader temperature range (see Movie S2 in the Supplemental Material [7], which was taken with an exposure time of 0.5 s for each PEEM image and with the temperature increment set at ca. 0.04 K). Figure 2 shows representative PEEM images and the change in the PE intensity. As the temperature increases, the transition begins at ca. 282 K in discrete segments and ends at ca. 290 K. Interestingly, the cracks nearly disappear and become almost invisible at a spatial resolution of 100 nm. The surface morphology closely resembles that one in the image before cooling [Fig. 1(a)]. This morphology change is a good indicator of the phase transition. A similar behavior but strain-induced morphology change is observed in a VO_2 film deposited on a TiO_2 substrate [16].

Phase transition is assessed by the anisotropic morphology change. This organic crystal was grown in a barlike shape with the stacking direction of EDO-TTF molecules on the long side of the crystal (*b* axis) [17], and the cracking cleaves across the EDO-TTF stacking column, i.e., in the *a*–*c* plane. Figures 3(a)–3(c) are the PEEM images taken from movie2_inc.mp4 at different specimen temperatures of 288.06, 289.38, and 289.86 K, respectively. For each image, the PE intensity profiles along the line A-B (parallel to *b* axis) and the line C-D (perpendicular to *b* axis) drawn in the PEEM images are shown in Figs. 3(d) and 3(e) in the corresponding colors. The black arrow in Fig. 3(d) indicates the position of the crack indicated by the black arrow in Fig. 3(a); this crack is brighter in Figs. 3(a) and 3(b) but darker in Fig. 3(c). Referencing this crack, the length along the *b* axis shrinks with increasing temperature. The movements of the cracks on both sides of the flake are indicated by the red, green, and blue arrows in Fig. 3(d). These two cracks are indicated with the white arrows in Fig. 3(b). While the groove is open in the low-temperature (LT) phase in Fig. 3(a), leading to a dark contrast at the flake edges that corresponds to around 2 μm on the horizontal axis of Fig. 3(b), the groove is closed in Figs. 3(b) and 3(c), exhibiting a bright contrast instead. The width of the flake, left-hand side of the black arrow, shrinks from ca. 6.6 to 6.3 μm from Figs. 3(a) to 3(b), which is as

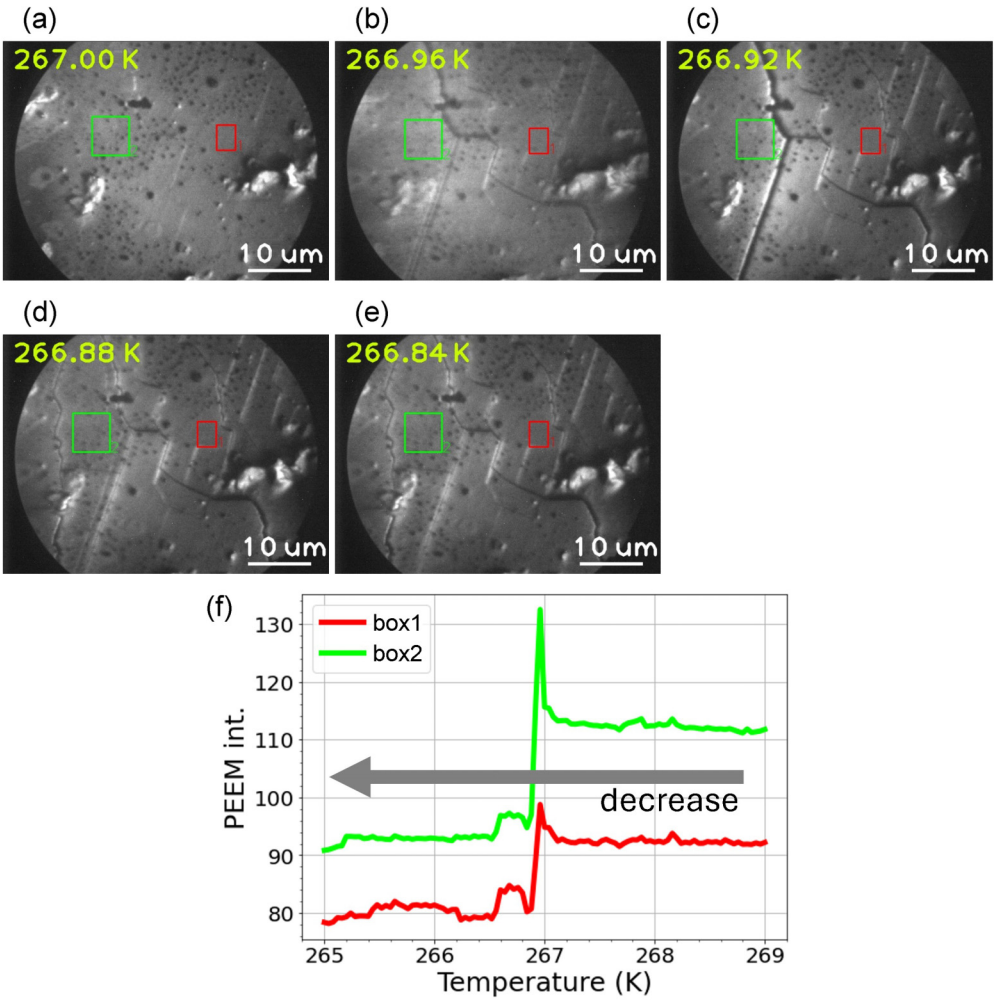

FIG. 1. Phase transition during cooling. PEEM images were acquired with an exposure time of 1 s while cooling the $(EDO\text{-}TTF)_2PF_6$ single crystal from 269 to 265 K (see Movie S1 in the Supplemental Material [7] for an associated movie). The excitation source was a Hg discharge lamp ($h\nu = 4.9$ eV), and the white bar corresponds to a length of 10 μm. During cooling, the crystal cracked at ca. 267 K because of the volume change, whereupon the phase transition occurred. Panels (a)–(e) show representative PEEM images during the transition, and panel (f) shows the temperature dependence of the average PE intensity in two regions indicated by the red and green boxes deduced from the PEEM images.

large as ca. 5%. On the other hand, neither expansion nor shrinkage was observed along the cracks (*a* axis), according to the intensity profiles along line C-D. The relatively large volume change compared with the lattice constant changes observed in Refs. [13,15] may arise from the higher transition temperature compared to the slow temperature increase. The phase transition took place at 290 K, which is approximately 10 K higher than the one reported in Refs. [13,14]. Furthermore, the inhomogeneity of transition temperature through the surface, and perhaps also in the depth direction, can be one reason of this inconsistency. Shrinkage by the transition of one part of the surface may widen cracks on another part where the transition does not occur yet. This behavior is actually observed in Movie S2 of the Supplemental Material [7]. The thermal hysteresis based on Figs. 1 and 2 is shown in Fig. S2 of the Supplemental Material; this resembles the hysteresis examined with the static magnetic susceptibility reported in Refs. [13,14]. Notably, this thermal hysteresis is repeatable.

III. ELECTRONIC STRUCTURES OF THE LT AND HT PHASES

Figures 1 and 2 show that the PE intensity changes during the transition, and below we explore the origin of this behavior both experimentally and theoretically.

To elucidate the energy dispersion around the Fermi level, PEEM images were acquired while sweeping the photon energy from 4.0 to 4.8 eV in steps of approximately 8 meV (see the Appendices A and B for details). Figure 4(a) shows spectra (PEEM intensity versus photon energy) measured at different specimen temperatures: 180, 258, and 300 K. In the LT phase at 180 K (green plot) and 258 K (red plot), the spectra are similar, both exhibiting a PE threshold of ca. 4.7 eV extrapolated from the linear region. In contrast, the spectrum for the high-temperature (HT) phase shows a different PE threshold at ca. 4.4 eV determined by linear fitting. This ca. 0.3 eV is consistent with the shift of the charge-transfer band observed in the infrared absorption spectra in Ref. [18]. The larger PE

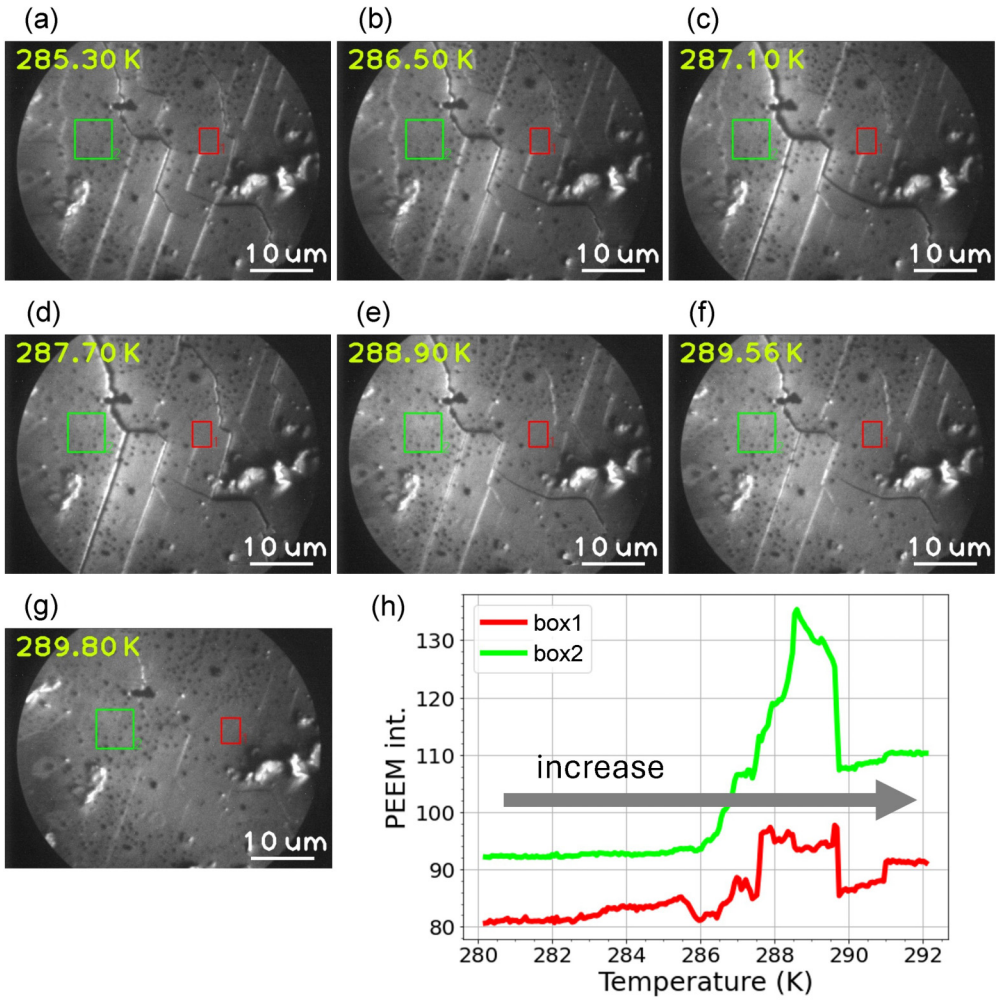

FIG. 2. Phase transition during heating. PEEM images were acquired with an exposure time of 0.5 s while heating the $(EDO\text{-}TTF)_2PF_6$ single crystal from 280 to 292 K (see Movie S2 in the Supplemental Material [7] for an associated movie). The excitation source was a Hg discharge lamp ($h\nu = 4.9$ eV), and the white bar corresponds to a length of 10 μm. Panels (a)–(g) show representative PEEM images taken during the transition, and panel (h) shows the temperature dependence of the average PE intensity in the red and green boxes deduced from the PEEM images.

intensity in the HT phase shown in Figs. 1 and 2 could be due to this additional PE from the tail part of the blue spectrum in Fig. 4(a).

Next, we sought to reproduce the spectra by means of first-principles calculations. The atomic configurations in the LT and HT phases [Figs. 4(c) and 4(e)] were obtained from density functional theory (DFT) calculations with the generalized gradient approximation (GGA) using experimentally determined lattice vectors [13], and the results were sufficiently close to the experimental observations. Using these configurations, the band dispersions and the DOS were calculated as shown in Fig. 4(b) for the LT phase and in Fig. 4(d) for the HT phase. The optimized atomic positions in the LT phase reproduce the charge density wave (CDW) electronic states in the GGA-PBE (Perdew-Burke-Ernzerhof) simulations. In the metallic band structure of the HT phase, the $\bar{\varphi}_1$ band crosses the Fermi energy, and a finite DOS at the Fermi energy contributes to tail states in the spectrum in Fig. 4(a). On the other hand, in the LT phase, EDO-TTF molecules are bent and $\bar{\varphi}_1$ in the HT phase splits into φ_1 and φ_2. This results in an opening of the gap at the Fermi energy, causing the tail to disappear in the spectrum. In this phase, among the low-energy bands, only the φ_1 band is unoccupied, while the φ_2, φ_3, and φ_4 bands are fully occupied. According to our simulation and Fig. 3 in Ref. [19], electrons in the φ_4 and φ_3 bands contribute to dimerization at LT. While in the φ_2 band, electrons having larger amplitudes in the bent molecules than the flat molecules contribute to form the charge order. In the DFT simulation, however, due to low reproducibility of the short-range correlation effects, the charge order is only partially reproduced. Above φ_1, there is an energy splitting on the order of 1 eV below the next excited state represented by ψ_1. This band is a σ antibonding band. When the electrons occupy this band, molecular deformation occurs. Three-dimensional maps of charge distributions (wave function profiles) for ψ_1, φ_1, φ_2, φ_3, and φ_4 are provided in Fig. S3 of the Supplemental Material [7] to visualize contributions to molecular bonding. Another dominant crystallographic change from the LT to HT phase is the rotation of PF_6 molecules, which is a result of the volume change as shown in Figs. 4(c) and 4(e).

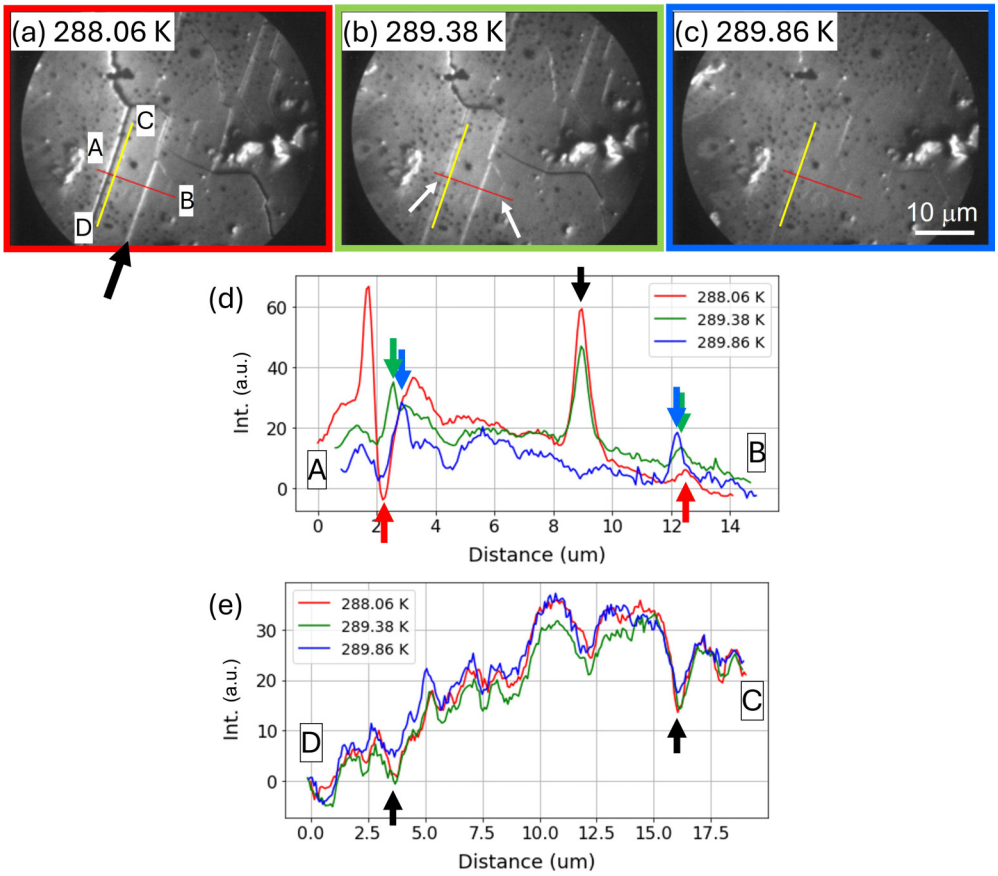

FIG. 3. (a)–(c) PEEM images acquired at sample temperature of 288.06, 289.38, and 289.86 K, respectively; the scale bar in panel (c) applies to all panels. (d) Intensity profiles along A-B in panel (a) to estimate the flake size. The black arrrow at 9 μm corresponds to the crack marked by the black arrow in panel (a). The flakes are ca. 6.6 μm wide in panel (a), shrinking to 6.3 μm in panel (c), a shrinkage of ca. 5%. (e) Intensity profiles along C-D in panel (a). No expansion or shrinkage was observed parallel to the crack.

IV. LIFETIME OF THE PHOTOEXCITED STATES

The crystallographic and electronic structures can also be modulated by photoirradiation. Figure 5(a) is a PEEM image obtained using a Hg lamp in the LT phase at 271 K, and as can be seen, the specimen was broken into micrometer-scale flakes. Upon laser irradiation with the parameters of 200 fs width, 1028 nm wavelength, 20 kHz repetition rate, and the fluence of 5 mJ/cm^2, the cracks are shrunk corresponding to the transition to the HT phase [Fig. 5(b)]. Compared with the temperature-dependent experiments reported in Figs. 1 and 2, the incomplete gap annihilation suggests the partial residue of LT phase especially in the underlying layers beyond the light penetration depth. The pumping wavelength corresponds to the charge-transfer gap observed in the optical spectra from Ref. [18]. Movie S3 in the Supplemental Material [7] was taken while the laser was switched on and off repeatedly, with an exposure time of 0.5 s per image. The pulse-to-pulse interval of 50 μs was too short to evacuate the photogenerated electrons, and this caused the specimen to remain in the HT phase while laser is on (see below).

To investigate PIPT, we captured PEEM images by a Hg discharge lamp during laser-pulse irradiation using the same laser source as that for Fig. 5(b) (pulse width: 200 fs; wavelength: 1028 nm, fluence: 5 mJ/cm^2) but varying the laser-pulse repetition rate in order to estimate the escape time of the photoexcited electrons and/or the heat. The repetition rate was adjusted from 20 kHz (which is sufficiently high for photogenerated electrons to accumulate) down to 0.05 kHz with the fluence kept constant. Subsequently, the laser shutter was closed at file number 230 and reopened at file number 260 at a rate of 10 kHz. The correspondence between file numbers and the repetition rate can be seen from Fig. 5(i). Figures 5(c)–5(h) show six PEEM images with the file number and the repetition rate from Movie S4 in the Supplemental Material [7]; as can be seen, by reducing the repetition rate from 20 kHz [Fig. 5(c)] to 0.1 kHz [Fig. 5(g)], the cracks widened. Figure 5(i) shows the repetition-rate-dependent PE intensity in the five regions marked in the PEEM images. With decreasing repetition rate, the PE intensity decreased because less electrons were accumulated, and this behavior is particularly evident in region 5 (black rectangle). Also, the decrement of the PE intensity is observed when the phase transition from the HT to the LT phase occurs in the regions 2 and 4. In the area around region 2 (green box), the specimen cracked when the repetition rate was changed from 0.2 to 0.1 kHz (at file number 190), and also the PE intensity decreased because of changes in the electronic structure, as observed in Figs. 1 and 2. Similarly, in region 4, the PE intensity decreased when the repetition rate was changed from 1 to 0.5 kHz. These

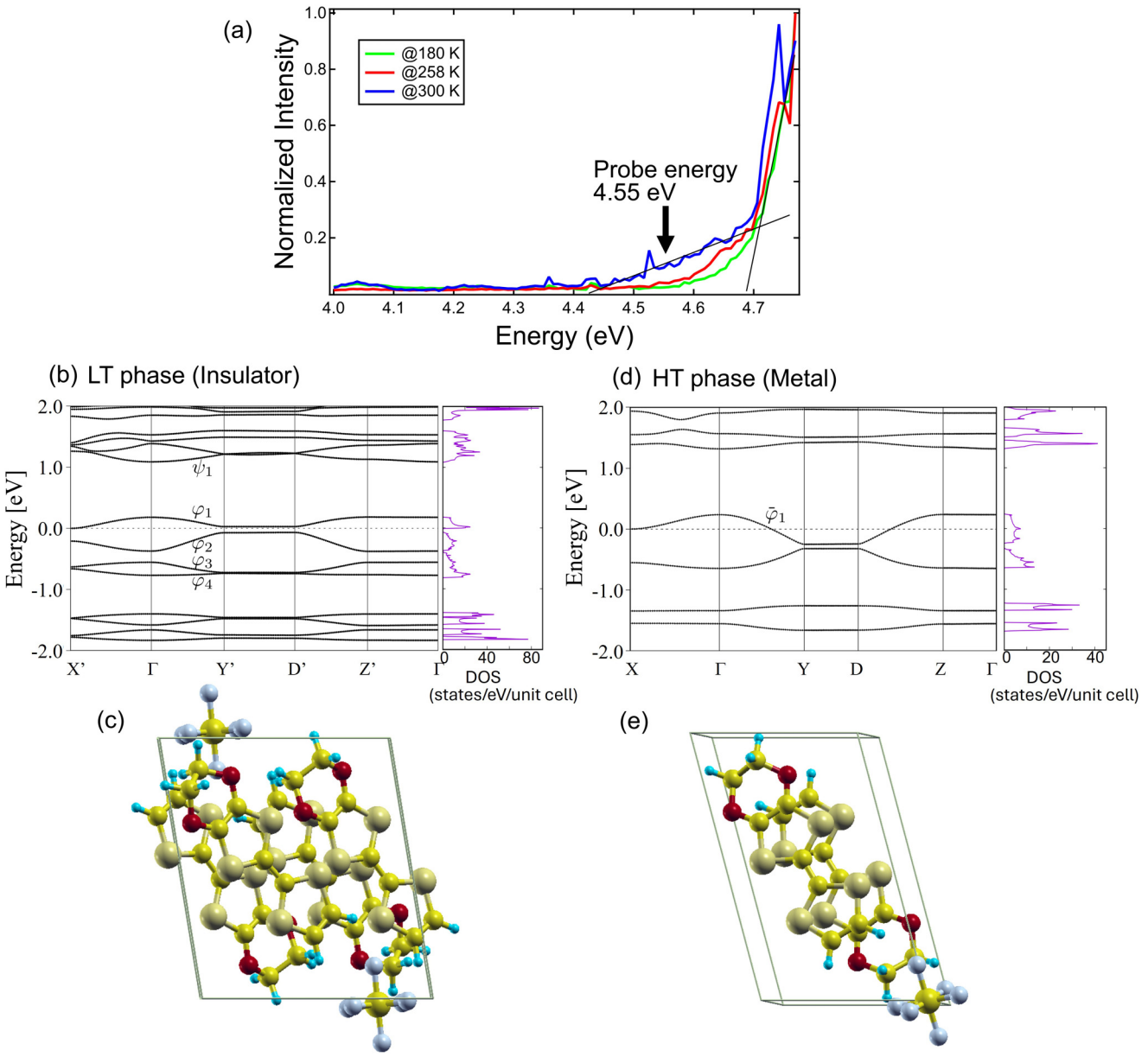

FIG. 4. (a) Spectra at 180, 258, and 300 K obtained by acquiring PEEM images while sweeping the photon energy from 4 to 4.8 eV in steps of approximately 8 meV; the PE threshold changed from 4.7 eV in the LT phase to 4.4 eV in the HT phase. (c), (e) Atomic configurations in the LT and HT phases obtained from calculations based on density functional theory with the generalized gradient approximation using experimentally determined lattice vectors, respectively [13]; the unit cell contains four EDO-TTF molecules in panel (c) and two in panel (e). (b), (d) Band dispersions and density of states (DOS) in (b) LT and (d) HT phases as simulated by first-principles calculations.

observations confirm that electron accumulation induces the phase transition, indicating that the transition can be controlled not only by temperature but also by photoirradiation. In this region, the morphology change was evaluated as shown in Fig. S4 of the Supplemental Material [7]. Changing the repetition rate from 0.2 to 0.1 kHz meant fewer accumulated electrons; therefore, when switching to the LT phase, the specimen expanded along the *b* axis, consistent with the thermally induced transition. The lifetime of photoinduced metallic phase varied from 1 to 5 ms (at most, 10 ms) across the different regions, and the transition was not homogeneous across the sample surface.

V. IMAGING ULTRAFAST PIPT

In this section, we show the results of imaging the phase transition induced only by the dynamics of the photoexcited electrons rather than by a thermal process. The phase transition in $(EDO\text{-}TTF)_2PF_6$ results in the volume change associated with the crystallographic structure change (bending or flattening of EDO-TTF molecules). Although this is a small crystallographic change, it has been measured by x-ray crystal structure analysis (using x-ray diffraction) [13]. Electron diffraction experiments in the time-resolved mode can observe the time-dependent charge-order melting process on a femtosecond timescale, but the number of diffraction

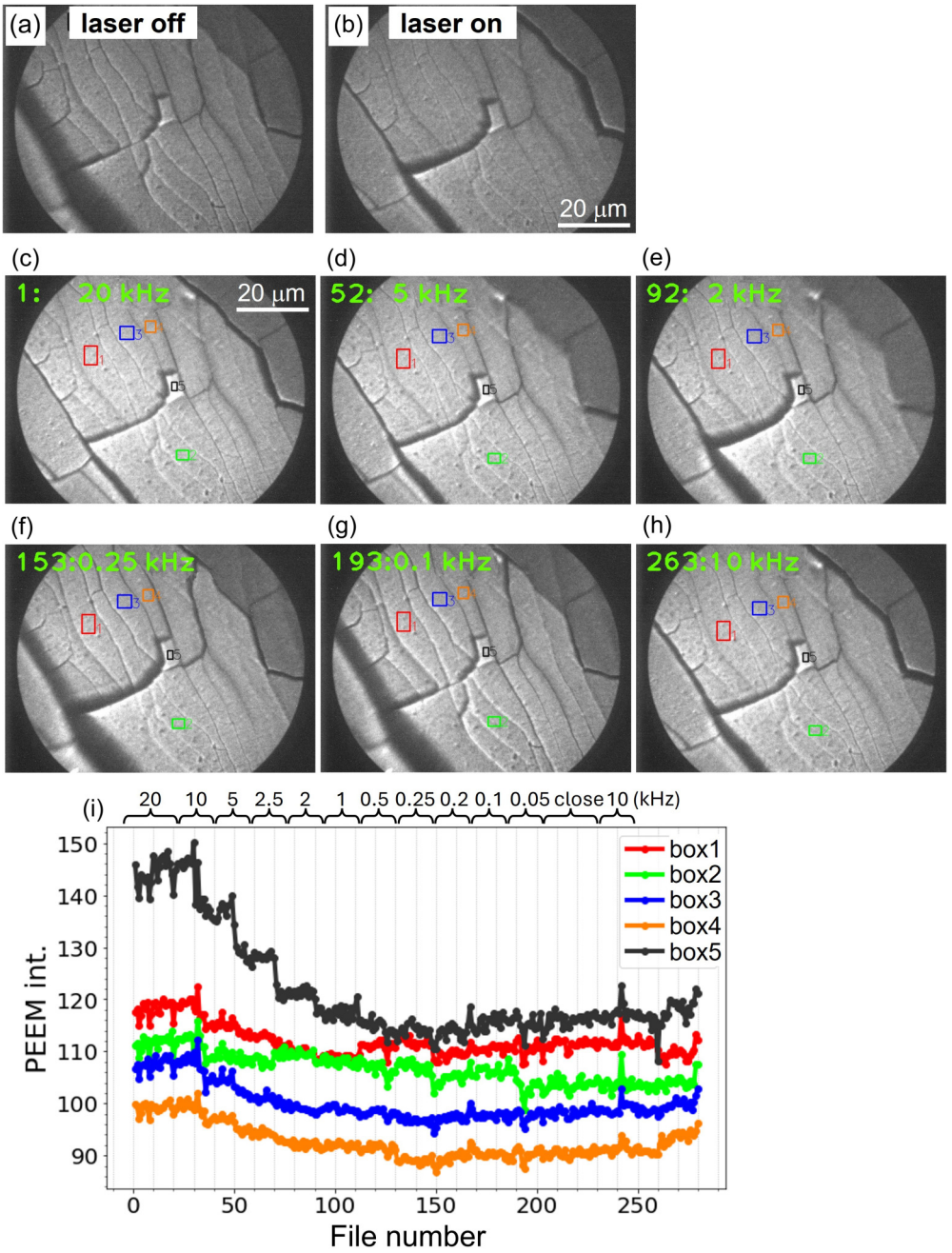

FIG. 5. Repetition rate dependence on phase transition: (a), (b) PEEM images obtained using a Hg discharge lamp with the pump laser on or off (wavelength: 1028 nm; repetition rate: 20 kHz); (c)–(h) representative PEEM images from the movie made while the laser repetition rate was changed from 20 to 0.05 kHz, after which the laser shutter was opened and closed with a repetition rate of 10 kHz (see Movie S4 in the Supplemental Material [7]); and (i) variation of the PE intensity in the five rectangular regions in the PEEM images. The sample temperature was 271 K.

data was not sufficient to capture small structural changes [15]. Also, the inhomogeneous nature of PIPT impedes signal detection, hindering the observation of volume changes essential for sensor and actuator applications. Therefore, we conducted PEEM experiments with an optical pump-probe scheme (time-resolved PEEM, TR-PEEM) to visualize the dynamics of the photoexcited electrons and the subsequent morphology change in real space.

Time-dependent PEEM images were acquired at a sample temperature of 268 K and in the time domain from −2 to 4 ps in steps of 0.1 ps; the repetition rate was 2 kHz by considering the results in Fig. 5 to have sufficient photoemission signal. While it is too short to suppress the accumulation of excited electrons, the relaxation to the metallic state was observed with this condition (see the last paragraph in this section). Figures 6(a)–6(e) show five images acquired at various pump-probe delay times ($\Delta t = -1.4$, 0.1, 0.8, 1.5, and 4.0 ps); these images were divided by a PEEM image captured at $\Delta t = -1.5$ ps in order to emphasize the morphology change. At $\Delta t = 0.1$ ps [Fig. 6(b)], a brighter region with a

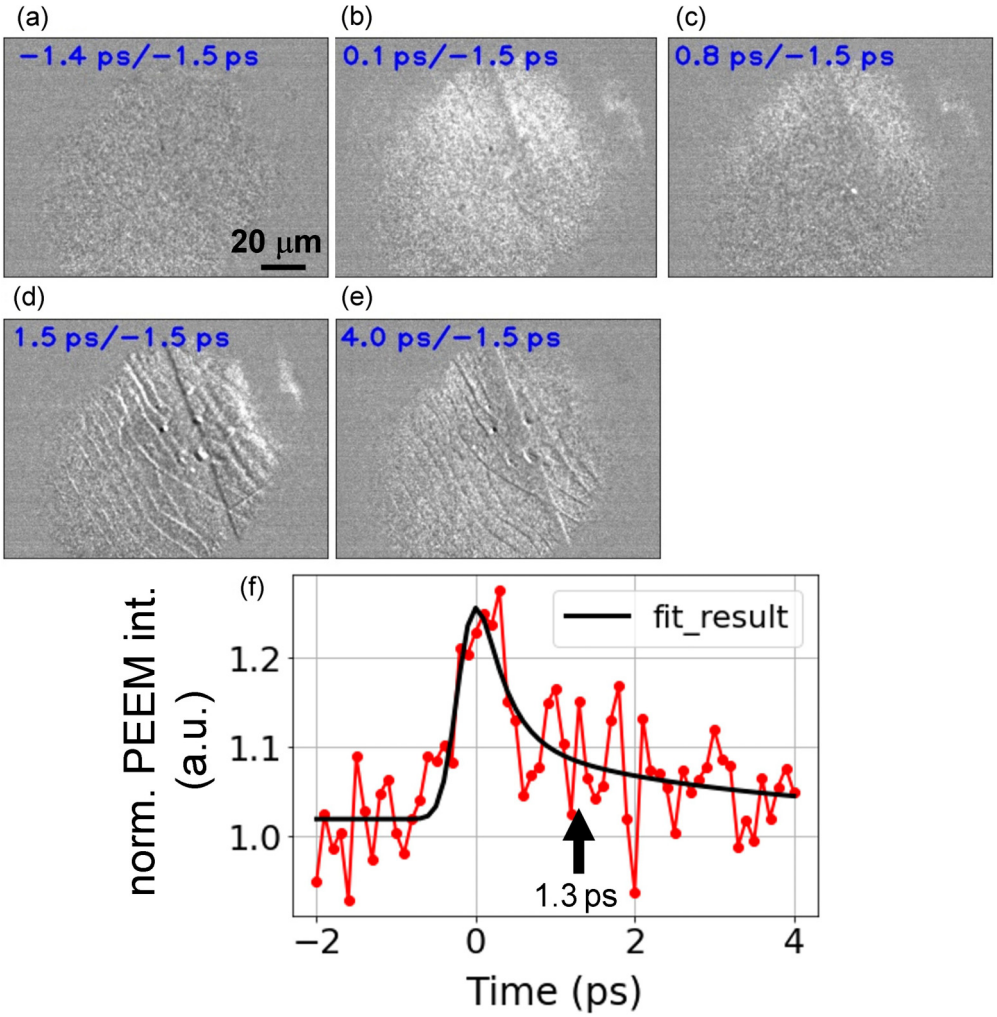

FIG. 6. Imaging of ultrafast PIPT in time-resolved PEEM experiments. The probe pulse had an energy of 4.55 eV, which was sufficient to induce PE from the HT phase, as indicated by the black arrow in Fig. 4(a). The pump pulse had an energy of 1.2 eV, and its size is 80 μm in diameter, which is estimated as 2σ, where σ is the standard deviation obtained from a Gaussian fit to panel (b). The sample temperature was 268 K, being in the LT phase. The repetition rate was 2 kHz to ensure a sufficiently long pulse-to-pulse interval. Δt was swept from −2 to 4 ps in steps of 0.1 ps. (a)–(e) PEEM images acquired at $\Delta t = -1.4$, 0.1, 0.8, 1.5, and 4.0 ps, divided by PEEM image acquired at $\Delta t = -1.5$ ps; the scale bar in panel (a) applies to all panels from panel (b) to panel (e). (f) Variation of the PE intensity normalized to the unpumped PEEM image as a function of Δt (red data points); the black curve is a numerical fit with the convolution of two exponential functions and a Gaussian function with a full width at half maximum of 400 fs (corresponding to the convolution of the pump and probe pulses).

diameter of about 80 μm appeared within the 130 μm PEEM field of view. This spatial profile corresponds to the shape of the pump pulse (i.e., the distribution of excited electrons) on the specimen surface. The red plots in Fig. 6(f) show the evolution of PE intensity with Δt. The numerical fitting using the convolution of a double-exponential function and a Gaussian function with a full width at half maximum (FWHM) of 0.4 ps yields time constants of $\tau_1 = 0.44 \pm 0.35$ ps and $\tau_2 = 3.2 \pm 3.6$ ps (the black curve). The faster dynamics correspond to the electron-lattice thermalization in the excited states, which completes at ca. at 1.3 ps, indicated by the black arrow in Fig. 6(f). Interestingly, the PEEM images start to change after this electron accumulation. This could be due to the change of surface potential induced by the change of charge density distribution and interatomic energy discussed in Sec. VI and also in Ref. [15]. The second time constant is assumed to be long, on the order of 20–100 ps, as observed in Refs. [15,18]. The plot in Fig. 6(f) lacks fitting accuracy due to a low signal-to-noise ratio after thermalization. Indeed, the chi-square value remains nearly unchanged even when the second time constant is varied longer than 3.5 ps up to 100 ps. Movie S5 in the Supplemental Material [7] shows the dynamics of morphology change together with the dynamics of photoexcited electrons [Fig. 6(f)].

As shown in Fig. 5, the phase transition caused by electron accumulation varied from flake to flake, and the cracks were not completely closed. Figure 7 highlights the ultrafast volume change focusing on one region. Figures 7(a)–7(c) show TR-PEEM images at $\Delta t = 1.2$, 1.5, and 1.8 ps, respectively. Figures 7(d) and 7(e) show the intensity profiles obtained from Figs. 7(a)–7(c) along lines A-B and C-D in Fig. 7(a). The molecular stacking axis extends along the *b* axis

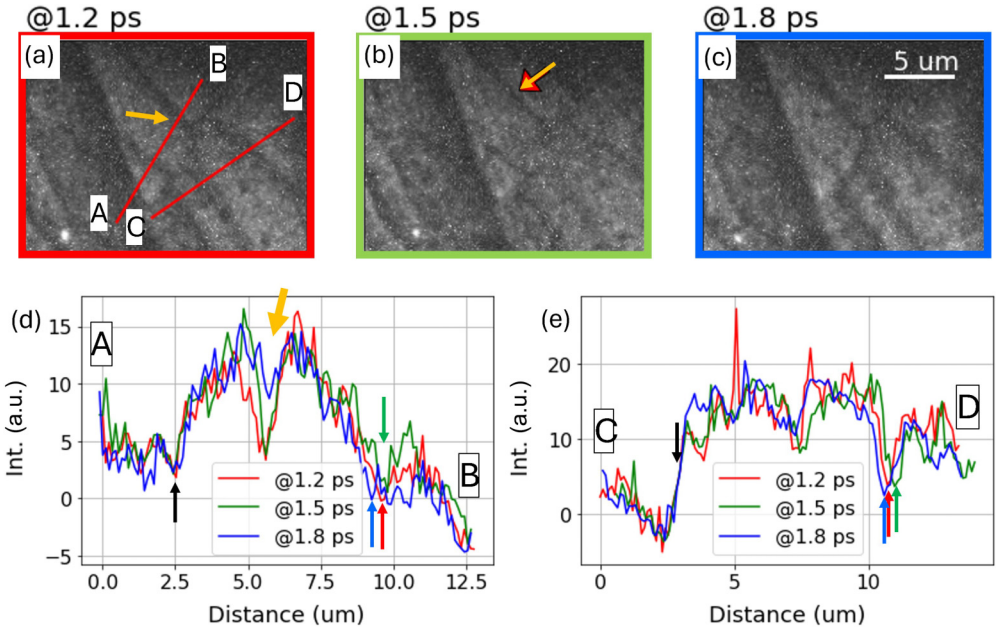

FIG. 7. (a)–(c) TR-PEEM images at $\Delta t = 1.2$, 1.5, and 1.8 ps extracted from the experiment in Fig. 6 but without division by image at −1.5 ps. (d), (e) PE intensity profiles along lines A-B and C-D extracted from panels (a)–(c). The lines are indicated in panel (a). The crack indicated by the orange arrows in panels (a) and (b) appears as a dip in the PEEM intensity, as indicated by the orange arrow in panel (d).

ca. 1% (∼50 nm) in 1.2–1.5 ps. Such large morphology changes induced by optical excitation have been reported in Refs. [20–22], which generates broadband phonons and leads to mechanical stress. Then, the structure relaxed slightly after $\Delta t = 1.5$ ps, with no recognizable motion up to 4 ps in the time window. This slower dynamics corresponds to the diffusive heating, which is also the so-called transient intermediate state in Refs. [15,18]. In this transient state, the large charge fluctuations screen the intermolecular forces, and the electron and lattice dynamics are locked. Note that the spatial resolution did not deteriorate during the time-resolved experiments, indicating that the pump-pulse irradiation triggered the phase transition in the flakes and the dynamics were reproduced by each pump pulse.

Further experiments were performed with a lower pump fluence (ca. one-third). The thermalization of the photoexcited electrons was 400 fs, but the relaxed electrons did not cause the system to enter the transient intermediate state. Therefore, the decay with the longer timescale was not observed, nor was any structural change (see Movie S6 in the Supplemental Material [7]), and the energy accumulated by each single pump pulse was insufficient for PIPT. In another experiment with a higher repetition rate of 20 kHz and the same pulse fluence as in the experiments in Fig. S5 of the Supplemental Material [7], the electron dynamics with the fast and slow decays were observed, but not structural dynamics (Figs. S5–S7 of the Supplemental Material, but only a slight motion as marked with the yellow ellipse in Fig. S7(f) of the Supplemental Material [7]). The pulse-to-pulse interval was too short for the system to relax, as examined in Fig. 5. These experiments confirmed PIPT in this compound and the presence of a threshold fluence between 1.7 and 5 $\mathrm{mJ/cm^2}$ at a wavelength of 1028 nm with 400 fs pulse width.

VI. SIMULATING PIPT

Here, we use first-principles calculations to explain the mechanism for the huge and ultrafast volume change of $(EDO\text{-}TTF)_2PF_6$. The band structure and DOS of the LT phase are shown in Fig. 4(b) and again in Fig. 8(a). In this phase, φ_2, φ_3, and φ_4 are filled with electrons, and the system is stable. We now move one electron from φ_2 to ψ_1 ca. 1 eV above the Fermi energy in order to demonstrate photoexcitation [Fig. 8(c)], and then the system becomes unstable. φ_2 is the highest occupied molecular orbital (HOMO) contributing to form the charge density wave, and ψ_1 is the σ antibonding bond, which shapes the framework of the molecule. To obtain the charge distribution $n(\mathbf{r})$ of excited electrons in a unit cell, we used a Gamma-point-only simulation; by fixing the electron occupation representing the charge-excited state (i.e., an electron in ψ_1 and a hole in φ_2), we evaluated changes in $n(\mathbf{r})$. As can be seen, there is no drastic change in the band structure from Figs. 8(a) to Fig. 8(c). However, the elements change regarding the electron contributions for the interatomic forces, and the residual forces appear instantaneously after photoexcitation. Consequently, the molecules store the internal energy, as indicated by the green arrows in Fig. 8(d). The most dominant force is to stretch the C=C bond connecting the sulfur rings at the middle of EDO-TTF. This energy is dissipated in the molecule and induced molecular motion such as flattening and sliding EDO-TTFs and rotating PF_6, as observed in Ref. [15].

The excitation of the internal energy was observed experimentally by means of time-resolved measurements of vibrational spectra. According to Matsubara *et al.*, the charge-ordering transition happens within 40 fs [23]; the subsequent energy relaxation excites the inter- and intramolecular vibrational modes within 100 fs to 1 ps, and this results in the

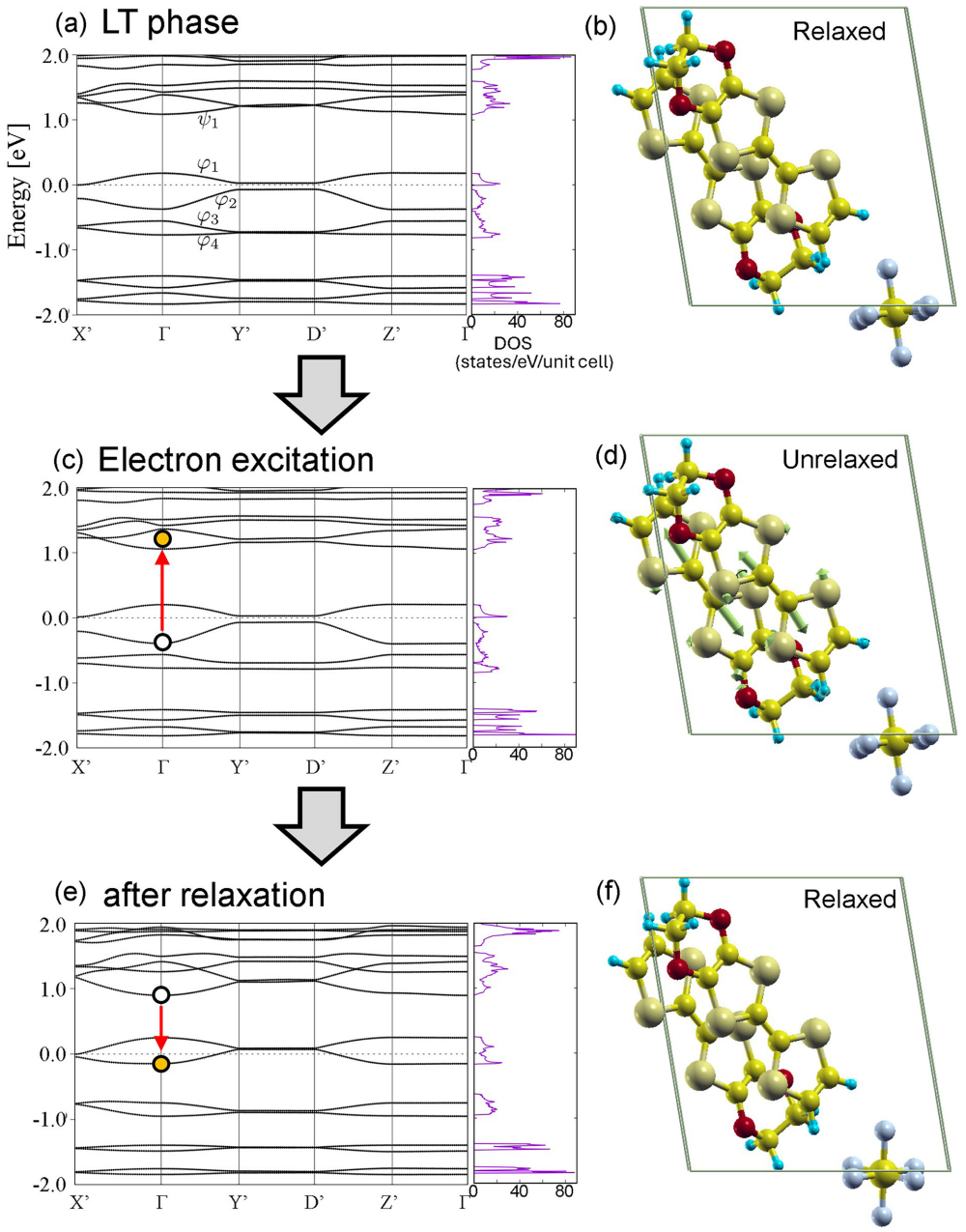

FIG. 8. Simulating PIPT by means of first-principles calculations: (a) band structure of the LT phase [same as Fig. 4(b), but only two EDO-TTF molecules are shown]; (c), (d) band structures just after photoexcitation and recombination, respectively; and (b), (d), (f) crystallographic structures [the green arrows in panel (d) indicate generated interatomic force vectors].

broadening of the vibrational spectra [24]. This appeared as the internal energy in our calculations, and this internal energy may initiate the volume change, i.e., PIPT.

The above suggests modification of the crystallographic structure in the excited state. Therefore, it was possible to determine the optimized atomic arrangement with the electron-hole pair, and the relaxed structure shown in Fig. 8(f) was obtained from calculations with the excited electron configuration. The internal energy induces molecular deformations. One of them is flattening the EDO-TTF molecules, which works as the dominant mechanism to induce the metallic band structure [Fig. 8(e)]. After the instantaneous volume change, the electron-hole pair recombines, and the system relaxes energetically to the transient intermediate state.

The validity of this picture is confirmed by calculations that take into account corrections for intermolecular van der Waals forces in addition to the volume changes, the so-called wannirization. We used GGA-PBE with the DFT-D3 corrections [25,26]. Structural relaxation calculations for the excited state with doubled CDW period confirm that metallization occurs with volume reduction, which generates lattice distortion, even when the excited electron density is halved. The results of the wannierization are shown in Fig. S8 of the Supplemental Material [7].

Wannierized ϕ_1 and ϕ_2 bands of the LT phase [Fig. S8(b) of the Supplemental Material [7]] suggest a mechanism of the deformation of EDO-TTF molecules caused by the CDW formation. The Wannier orbital of this isolated ϕ_1 band indicates an intermolecular antibonding character [Fig. S9(a) of the Supplemental Material [7]]. The orbital is well localized in a bent bimolecular pair [Fig. S9(b) of the Supplemental Material [7]]. In the CDW phase that occurs at 3/4 filling, local molecular distortion happens inside the crystal as a result of electron occupation of the intermolecular antibonding orbitals. In other words, in the LT-CDW phase, when two neutral molecules form a pair, the π bond between them weakens, and the five-membered ring in one of molecules becomes repulsive relative to another neighboring ring of the other molecule. As a result, by exciting the electron in the ϕ_2 band and leaving the Wannier orbital empty, the molecule regains its flatness, resulting in a metallization accompanied by a volume reduction.

VII. CONCLUSIONS

In the study reported here, we explored phase transitions in the organic charge-transfer complex (EDO-TTF)$_2$PF$_6$. The transitions induced by temperature variation and photoirradiation were verified via PEEM, enabling the visualization of morphological changes such as cracking, as well as the differences in spectral shapes and PE intensity between the LT and HT phases. Moreover, we observed pure PIPT by capturing the dynamics of the photoexcited electrons and the subsequent volume change with resolutions of 100 fs and 100 nm. We observed that photoexcited electrons relaxed to unoccupied states within 1.3 ps, and first-principles calculations showed that the accumulated excited electrons generate internal energy and force imbalances that cause a transition in the electronic states accompanied by a volume change, thereby initiating PIPT.

ACKNOWLEDGMENTS

This work was supported by JST CREST "Developing a fusion of optical science and technology using advanced light sources," research area "Critical non-equilibrium material exploration led by light technology," MEXT Q-LEAP Attosecond lasers for next frontiers in science and technology (ATTO), JSPS KAKENHI (15K17677, 17H06141, 17H06372, 21H01752, 23H01977, 23H04631, 23K20039, 23H00269, and 25H01260), and JST FOREST Program, Grant No. JPMJFR203P.

DATA AVAILABILITY

The experimental data that support the findings of this article are openly available. Requests for the simulation data and further information should be sent to the authors.

APPENDIX A: SUMMARY OF FEMTOSECOND PHOTOELECTRON EMISSION MICROSCOPY

Figure 9 shows schematically the optics that were used in the fs-PEEM equipment. A femtosecond laser system (Pharos SP; Light Conversion Co. Ltd.) was used in this study. The fundamental wavelength of the light was 1028 nm ($h\nu$ = 1.2 eV), the pulse width was 190 fs, and the repetition rate was tunable from single shot to 500 kHz. The maximum output power was 6 W, and for this study the laser system was optimized to 6 W at 20 kHz, i.e., 300 μJ per pulse. The repetition rate was tuned using an optical pulse picker with the same pulse fluence at different repetition rates. The laser pulses were guided to an optical parametric amplifier (OPA) (Orpheus; Light Conversion Co. Ltd.), and the wavelength was tunable from 2500 to 620 nm. The output power ranges from 200 to 400 mW depending on wavelength. After the OPA, four wave selectors were used to select idler light and signal light (namely, polarization) and also the wavelength, band two mirrors for the laser path back to the original axis. Nonlinear crystals (β-BaB_2O_4) were then used to generate the second and fourth harmonics. Finally, the wavelength was tunable from 2500 to 210 nm, i.e., a photon energy of 0.5–5.9 eV. In this study, UV laser pulses in the range of 4–4.8 eV were used to induce photoelectron emission, and these pulses were the probe pulses. Part of the energy that was not used for the OPA was used as pump pulses to excite the electrons in the specimen. The pump and probe pulses entered the ultrahigh-vacuum chamber via one of its view ports and illuminated the specimen; the timing of the pump and probe pulses for sample illumination was controlled by using an optical delay stage for the pump laser.

The PEEM equipment was supplied by FOCUS GmbH. An air lock was used to allow the introduction of samples from ambient air to ultrahigh vacuum, and a copper evaporator was mounted in the air-lock chamber.

APPENDIX B: OBTAINING SPECTRA USING FS-PEEM

In the fs-PEEM system, when the output wavelength is sent via a remote command, the wavelength of the OPA is tuned automatically in the range between 620 and 2500 nm, and the wave selectors and mirrors mounted on linear stages are positioned accordingly. One or two nonlinear crystals are also selected depending on the polarization of signal and idler pulses, and their angles are also adjusted. Additionally, filters and/or multilayer mirrors are inserted into the laser path to annihilate the fundamental and/or second harmonic laser beams. A neutral density filter was used to adjust the fluence, and a three-axis stage was synchronized to adjust the probe pulse position on the sample surface. Using this system, spectra were obtained from PEEM images acquired by sweeping the wavelength in a stepwise manner; at each step, the laser power was calibrated using a power meter to normalize the PE intensity. The energy resolution is defined by the energy width of the probe pulse, which was ca. 30 meV (FWHM).

APPENDIX C: TIME-RESOLVED MODE

The dynamics of the photogenerated electrons was observed by acquiring PEEM images with a stepwise sweep of the delay time between the pump and probe pulses (Δt). In

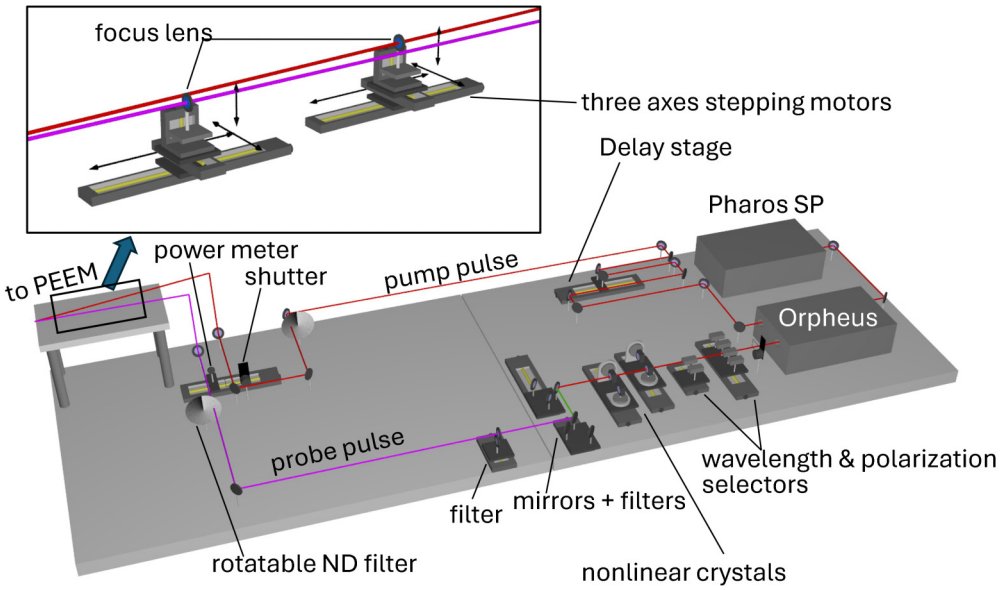

FIG. 9. A schematic of the optics for the fs-PEEM system.

this study, the photon energy of the probe pulse was 4.55 eV, which was just sufficient to induce PE from the HT metal phase denoted by the black arrow in Fig. 4(a). The pump pulse was 1.2 eV, and the fluence was 10 mJ/cm^2. Δt was swept from -2 to 4 ps in steps of 0.1 ps, and at each step a PEEM image was recorded with an exposure time of 10 s. PEEM images without pump pulses were also recorded at each step in order to eliminate background noise. The sample temperature was 268 K so as to be in the LT phase. The experiments were performed at repetition rates of 2 and 20 kHz, and the results for 2 kHz are shown in Fig. 6. The dynamics of the photoexcited electrons in Fig. 6(f) were obtained by averaging the PE intensity. The time constants of 400 fs and 3.5 ps or longer were extracted by numerical fitting using a convolution of two exponential curves and a Gaussian function with an FWHM of 400 fs.

APPENDIX D: FIRST-PRINCIPLES CALCULATIONS

DFT calculations were performed using the Quantum espresso package [27,28], with a PBE exchange-correlation functional [29] used with ultrasoft pseudopotentials [30] to describe the electronic interaction. In this study, the lattice vectors were fixed to those determined experimentally for the LT or HT phase as required [13], and no further optimization of the cell geometry was performed. A kinetic energy cutoff of 45 Ry was used for the wave functions, and a $2 \times 2 \times 2$ k-point grid was used for the structure optimization calculations, with a total force tolerance of 0.0001 eV/Å. To obtain the DOS, a finer $12 \times 12 \times 12$ k-point grid was used, along with the self-consistent charge density given by either a $2 \times 2 \times 2$ k-point mesh simulation for the ground-state calculation or a Gamma-point-only simulation for calculating the excited electron configuration.

[1] S. Koshihara, Y. Tokura, T. Mitani, G. Saito, and T. Koda, Photoinduced valence instability in the organic molecular compound tetrathiafulvalene-*p*-chloranil (TTF-CA), Phys. Rev. B **42**, 6853 (1990).

[2] H. Tokoro, M. Yoshikiyo, K. Imoto, A. Namai, T. Nasu, K. Nakagawa, N. Ozaki, F. Hakoe, K. Tanaka, K. Chiba, R. Makiura, K. Prassides, and S.-I. Ohkoshi, External stimulation-controllable heat-storage ceramics, Nat. Commun. **6**, 7037 (2015).

[3] Y. Kawakami, T. Fukatsu, Y. Sakurai, H. Unno, H. Itoh, S. Iwai, T. Sasaki, K. Yamamoto, K. Yakushi, and K. Yonemitsu, Early-stage dynamics of light-matter interaction leading to the insulator-to-metal transition in a charge ordered organic crystal, Phys. Rev. Lett. **105**, 246402 (2010).

[4] D. Loke, J. M. Skelton, W.-J. Wang, T.-H. Lee, R. Zhao, T.-C. Chong, and S. R. Elliott, Ultrafast phase-change logic device driven by melting processes, Proc. Natl. Acad. Sci. USA **111**, 13272 (2014).

[5] P. Naumov, S. C. Sahoo, B. A. Zakharov, and E. V. Boldyreva, Dynamic single crystals: Kinematic analysis of photoinduced crystal jumping (the photosalient effect), Angew. Chem. Int. Ed. **52**, 9990 (2013).

[6] T. Takeda, M. Ozawa, and T. Akutagawa, Jumping crystal of a hydrogen-bonded organic framework induced by the collective molecular motion of a twisted π system, Angew. Chem. Int. Ed. **58**, 10345 (2019).

[7] See Supplemental Material at http://link.aps.org/supplemental/10.1103/22k3-7nym for the experimental and simulation details.

[8] T. Danz, T. Domröse, and C. Ropers, Ultrafast nanoimaging of the order parameter in a structural phase transition, Science **371**, 371 (2021).

[9] A. S. Johnson, D. Perez-Salinas, K. M. Siddiqui, S. Kim, S. Choi, K. Volckaert, P. E. Majchrzak, S. Ulstrup, N. Agarwal, K. Hallman, *et al.*, Ultrafast X-ray imaging of the light-induced phase transition in VO_2, Nat. Phys. **19**, 215 (2023).

[10] M. A. Huber, M. Plankl, M. Eisele, R. E. Marvel, F. Sandner, T. Korn, C. Schüller, R. F. Haglund Jr., R. Huber, and T. L. Cocker, Ultrafast mid-infrared nanoscopy of strained vanadium dioxide nanobeams, Nano Lett. **16**, 1421 (2016).

[11] K. Fukumoto, Y. Yamada, K. Onda, and S. Koshihara, Direct imaging of electron recombination and transport on a semiconductor surface by femtosecond time-resolved photoemission electron microscopy, Appl. Phys. Lett. **104**, 053117 (2014).

[12] R. Hayakawa, S. Takeiri, Y. Yamada, Y. Wakayama, and K. Fukumoto, Carrier transport mechanism in organic antiambipolar transistors unveiled by operando photoemission electron microscopy, Adv. Mater. **34**, 2201277 (2022).

[13] A. Ota, H. Yamochi, and G. Saito, A novel metal-insulator phase transition observed in (EDO-TTF)$_2$PF$_6$, J. Mater. Chem. **12**, 2600 (2002).

[14] Y. Nakano, H. Yamochi, G. Saito, M. Uruichi, and K. Yakushi, Anion size and isotope effects in (EDO-TTF)$_2$XF$_6$, J. Phys.: Conf. Ser. **148**, 012007 (2009).

[15] M. Gao, C. Lu, H. Jean-Ruel, L. C. Liu, A. Marx, K. Onda, S.-y. Koshihara, Y. Nakano, X. Shao, T. Hiramatsu, G. Saito, H. Yamochi, R. R. Cooney, G. Moriena, G. Sciaini, and R. J. D. Miller, Mapping molecular motions leading to charge delocalization with ultrabright electrons, Nature (London) **496**, 343 (2013).

[16] J. Krisponeit, S. Fischer, S. Esser, V. M. Moshnyaga, T. Schmidt, L. F. J. Piper, J. I. Flege, and J. Felta, The morphology of $VO_2/TiO_2(001)$: Terraces, facets, and cracks, Sci. Rep. **10**, 22374 (2020).

[17] M. Sakata, M. Maesato, A. Ota, H. Yamochi, and G. Saito, Uniaxial strain investigation on the metal-insulator transition of (EDO-TTF)$_2$PF$_6$, Synth. Met. **153**, 393 (2005).

[18] K. Onda, S. Ogihara, K. Yonemitsu, N. Maeshima, T. Ishikawa, Y. Okimoto, X. Shao, Y. Nakano, H. Yamochi, G. Saito, and S. Y. Koshihara, Photoinduced change in the charge order pattern in the quarter-filled organic conductor (EDO-TTF)$_2$PF$_6$ with a strong electron-phonon interaction, Phys. Rev. Lett. **101**, 067403 (2008).

[19] G.-J. Linker, P. H. M. van Loosdrecht, P. T. van Duijnen, and R. Broer, Periodic Hartree-Fock and hybrid density functional calculations on the metallic and the insulating phase of (EDO-TTF)$_2$PF$_6$, Phys. Chem. Chem. Phys. **17**, 30371 (2015).

[20] M. Fiebig, K. Miyano, Y. Tomioka, and Y. Tokura, Subpicosecond photo-induced melting of a charge-ordered state in a perovskite manganite, Appl. Phys. B **71**, 211 (2000).

[21] M. Fiebig, K. Miyano, Y. Tomioka, and Y. Tokura, Reflection spectroscopy on the photoinduced local metallic phase of $Pr_{0.7}Ca_{0.3}MnO_3$, Appl. Phys. Lett. **74**, 2310 (1999).

[22] D. E. Cox, P. G. Radaelli, M. Marezio, and S.-W. Cheong, Structural changes, clustering, and photoinduced phase segregation in $Pr_{0.7}Ca_{0.3}MnO_{0.3}$, Phys. Rev. B **57**, 3305 (1998).

[23] Y. Matsubara, S. Ogihara, J. Itatani, N. Maeshima, K. Yonemitsu, T. Ishikawa, Y. Okimoto, S.-y. Koshihara, T. Hiramatsu, Y. Nakano, H. Yamochi, G. Saito, and K. Onda, Coherent dynamics of photoinduced phase formation in a strongly correlated organic crystal, Phys. Rev. B **89**, 161102(R) (2014).

[24] N. Fukazawa, M. Shimizu, T. Ishikawa, Y. Okimoto, S.-Y. Koshihara, T. Hiramatsu, Y. Nakano, H. Yamochi, G. Saito, and K. Onda, Charge and structural dynamics in photoinduced phase transition of (EDO-TTF)$_2$PF$_6$ examined by picosecond time-resolved vibrational spectroscopy, J. Phys. Chem. C **116**, 5892 (2012).

[25] S. Grimme, J. Antony, S. Ehrlich, and H. Krieg, A consistent and accurate *ab initio* parametrization of density functional dispersion correction (DFT-D) for the 94 elements H–pu, J. Chem. Phys. **132**, 154104 (2010).

[26] S. Grimme, S. Ehrlich, and L. Goerigk, Effect of the damping function in dispersion corrected density functional theory, J. Comput. Chem. **32**, 1456 (2011).

[27] P. Giannozzi, S. Baroni, N. Bonini, M. Calandra, R. Car, C. Cavazzoni, D. Ceresoli, G. L. Chiarotti, M. Cococcioni, I. Dabo, *et al.*, Quantum ESPRESSO: A modular and open-source software project for quantum simulations of materials, J. Phys.: Condens. Matter **21**, 395502 (2009).

[28] P. Giannozzi, O. Andreussi, T. Brumme, O. Bunau, M. B. Nardelli, M. Calandra, R. Car, C. Cavazzoni, D. Ceresoli, M. Cococcioni, *et al.*, Advanced capabilities for materials modelling with Quantum ESPRESSO, J. Phys.: Condens. Matter **29**, 465901 (2017).

[29] J. P. Perdew, K. Burke, and M. Ernzerhof, Generalized gradient approximation made simple, Phys. Rev. Lett. **77**, 3865 (1996).

[30] A. M. Rappe, K. M. Rabe, E. Kaxiras, and J. D. Joannopoulos, Optimized pseudopotentials, Phys. Rev. B **41**, 1227 (1990).